

3D DENSITY-GRADIENT BASED EDGE DETECTION ON NEURAL RADIANCE FIELDS (NERFS) FOR GEOMETRIC RECONSTRUCTION

Miriam Jäger*, Boris Jutzi

Institute of Photogrammetry and Remote Sensing, Karlsruhe Institute of Technology, Germany
(miriam.jaeger, boris.jutzi)@kit.edu

KEY WORDS: Neural Radiance Fields, Density Field, Density Gradient, Sobel, Canny, Laplacian of Gaussian, 3D Reconstruction

ABSTRACT:

Generating geometric 3D reconstructions from Neural Radiance Fields (NeRFs) is of great interest. However, accurate and complete reconstructions based on the density values are challenging. The network output depends on input data, NeRF network configuration and hyperparameter. As a result, the direct usage of density values, e.g. via filtering with global density thresholds, usually requires empirical investigations. Under the assumption that the density increases from non-object to object area, the utilization of density gradients from relative values is evident. As the density represents a position-dependent parameter it can be handled anisotropically, therefore processing of the voxelized 3D density field is justified. In this regard, we address geometric 3D reconstructions based on density gradients, whereas the gradients result from 3D edge detection filters of the first and second derivatives, namely Sobel, Canny and Laplacian of Gaussian. The gradients rely on relative neighboring density values in all directions, thus are independent from absolute magnitudes. Consequently, gradient filters are able to extract edges along a wide density range, almost independent from assumptions and empirical investigations. Our approach demonstrates the capability to achieve geometric 3D reconstructions with high geometric accuracy on object surfaces and remarkable object completeness. Notably, Canny filter effectively eliminates gaps, delivers a uniform point density, and strikes a favorable balance between correctness and completeness across the scenes.

1. INTRODUCTION

Neural Radiance Fields (NeRFs) (Mildenhall et al., 2020) pioneered computer graphics and computer vision by enabling the rendering of novel views through view synthesis from neural networks. These networks estimate density and color values for each position in 3D space based on input image data and camera poses. Generating accurate and complete 3D reconstructions from Neural Radiance Fields (NeRFs) is of interest in the field of photogrammetry. Through the utilization of estimated density values, NeRF based 3D reconstructions are possible. More precisely, by considering the density as a kind of pseudo-probability for the occurrence of an object in 3D space (Jäger et al., 2023).

Nevertheless, the filtering with global density thresholds is empirical and requires sufficient analysis of its geometric correctness. Accordingly, the 3D reconstruction depends on the chosen density threshold and often yields noisy and incomplete surfaces (Li et al., 2023; Wang et al., 2021). The assumption that the density increases from non-object to object area, motivates the processing of the 3D scene in terms of its density gradients. As the density represents a position-dependent parameter, it can be addressed anisotropically, justifying a ray-independent sampling. For this reason, we propose to perform geometric 3D reconstruction with respect to density gradients, while the key aspect is the utilization of 3D gradient filter for 3D edge detection. This allows the extraction of edges along a wide density range based on gradients of relative neighboring values.

We introduce a straightforward workflow for enabling geometric 3D reconstruction from NeRFs with the 3D density gradients based on the first and second derivative, while using gradient filter for edge detection in the voxelized 3D density field. In

order to evaluate the geometric accuracy and robustness of our framework, we address the DTU benchmark dataset (Jensen et al., 2014) with different types of real objects, which feature different sizes, structures, materials, textures and colors.

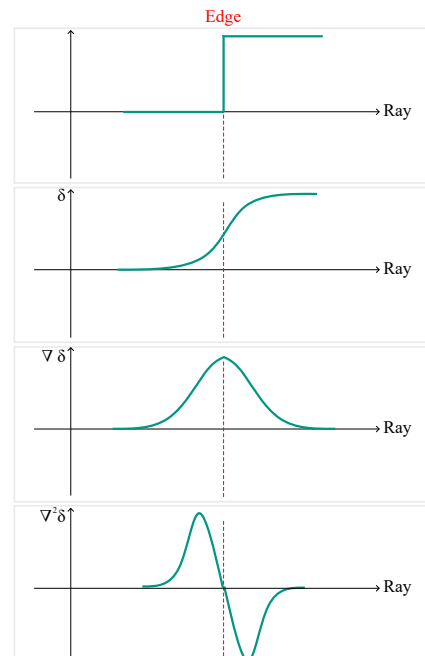


Figure 1. Density Gradient e.g. for 1D on a ray. The illustrations display the characteristics of the density values exemplarily as they would occur during ray tracing into the direction of an object. From top to bottom: An ideal edge in a binary non-object to object space, the raw density values, the first derivative of the density values (edge at the maximum), the second derivative of the density values (edge at the zero crossing).

* Corresponding author

2. RELATED WORK

In this section, we briefly summarize related work to our research. Firstly, we give an overview on basic, recent research and developments on NeRFs. Following this, we address recent research on neural surface reconstructions.

Neural Radiance Fields The foundation for Neural Radiance Fields (NeRFs) was established by Scene Representation Networks (SRNs) (Sitzmann et al., 2019). Their underlying principle is modeling the scene as a function of 3D coordinates within it. It was followed by the groundbreaking research work of Neural Radiance Fields (Mildenhall et al., 2020). The network enables the estimation of color and density values for each 3D position through 6D camera poses and associated 2D images by training a neural network with multi-layer perceptrons (MLPs).

The vanilla NeRF was followed by thousands of publications driving research and development in various domains. Scalability enhancements are demonstrated by Mega-NeRF (Turki et al., 2022) and Block-NeRF (Tancik et al., 2022), which employ data partitioning and the training of several NeRFs. Bundle Adjusting Radiance Fields (BaRF) (Lin et al., 2021) and Gaussian Activated Radiance Fields (GaRF) (Chng et al., 2022) address the task of a camera pose estimation. Dynamic contributions use time as an additional input dimension for time-dependent rendering (Pumarola et al., 2021) or for preventing the occurrence of artifacts due to dynamic pixels (Gao et al., 2021). Several Methods such as AdaNeRF (Kurz et al., 2022), FastNeRF (Garbin et al., 2021) and Instant NGP (Müller et al., 2022) focus on faster training or rendering. While Instant NGP uses a combination of small MLPs and spatial hash table encoding. Neuralangelo (Li et al., 2023) adapts Instant NGP and combines hash grids with neural surface rendering for high-fidelity surface reconstruction. Besides the neural methods, non-neural research like Plenoxels (Fridovich-Keil et al., 2022) have been introduced.

Neural Surface Reconstructions Regarding neural surface reconstructions Unisurf (Oechsle et al., 2021) learns implicit surfaces, by addressing the occupancy along rays. Several works such as NeuS (Wang et al., 2021) and VolSDF (Yariv et al., 2021) represent the scene by neural Signed Distance Functions (SDFs) (Park et al., 2019). Neuralwarp (Darmon et al., 2022) builds on VolSDF, whereas using Structure from Motion information to guide surface optimizations.

3. METHODOLOGY

Firstly, in Section 3.1 describes the principal motivation for density gradients underlying our framework. Secondly, in Section 3.2 and Section 3.3 the first and second derivative calculation for density gradients is explained. Finally, Section 3.4 outlines the evaluation process, which focuses on completeness and correctness.

3.1 Density Gradient

Reconstructions based on filtering the NeRFs density output by global density thresholds requires adaptive adjustments, since the density values behavior differ for various NeRFs, datasets, hyperparameters and network configurations. Accordingly, the 3D reconstruction depends on the chosen threshold and does not

provide optimal, noisy or incomplete reconstructions (Wang et al., 2021; Oechsle et al., 2021; Li et al., 2023).

Several previous works consider ray-based 3D reconstruction with NeRFs or SDFs (Oechsle et al., 2021; Wang et al., 2021; Darmon et al., 2022). Nevertheless, the density values in principle are anisotropic and position-dependent. For this reason, we propose to process the geometric 3D reconstruction in the dense voxelized 3D density field. With the aim of performing position-dependent 3D reconstructions, regardless of global density thresholds, we introduce 3D gradient filters. To identify edges characterized by variations in magnitudes, hence density values, we extend from two to the three-dimensional edge filter among the 3D density field. In doing so, the density gradients instead of the raw density values from NeRFs are regarded, since the density value increases towards the object. The extraction of the edges can rely on the first as well as the second derivative of the density, see Figure 1. Thereby, we guarantee anisotropy as well as the consideration of neighborhoods in the reconstruction process.

3.2 First Derivative

Edges in images as well as in 3D voxel space can be detected based on the first derivatives, i.e. the corresponding density gradients in this case.

Sobel filter We address the well-established Sobel filter (Sobel and Feldman, 1973) for edge detection, which performs a smoothing orthogonal to the first derivative. As the processing is done in the 3D density field, the 3D Sobel filter is built up of the following components for each direction x , y and z , e.g., for the x -direction for the central element (Sobel and Feldman, 1973):

$$s_{-1} = \begin{bmatrix} -1 & -2 & -1 \\ -2 & -4 & -2 \\ -1 & -2 & -1 \end{bmatrix}, s_0 = \begin{bmatrix} 0 & 0 & 0 \\ 0 & 0 & 0 \\ 0 & 0 & 0 \end{bmatrix}, s_1 = \begin{bmatrix} 1 & 2 & 1 \\ 2 & 4 & 2 \\ 1 & 2 & 1 \end{bmatrix}, \quad (1)$$

and delivers the density gradients $G_{\delta,x}$, $G_{\delta,y}$ and $G_{\delta,z}$ in direction x , y and z in the density field. The total Sobel gradient $\Delta_{\delta,\text{Sobel}}$ for each sample in the density field is further given by

$$\Delta_{\delta,\text{Sobel}} = \sqrt{G_{\delta,x}^2 + G_{\delta,y}^2 + G_{\delta,z}^2}. \quad (2)$$

Canny filter Furthermore, we address Canny filter (Canny, 1986) for 3D edge detection, while it offers an improved edge detection in contrast to the Sobel filter. The gradient calculation based on the density value, such as described for Sobel filter, is first preceded by a Gaussian smoothing in the 3D density field to suppress noise. This is followed by gradient magnitude thresholding with a lower and upper relative threshold on the density gradients for edge detection. Finally, a hysteresis method is used to track strong edges and suppress weak ones at the same time. The final density gradient values based on Canny filter are referred as $\Delta_{\delta,\text{Canny}}$ in the following. From this method, we expect to extract a wide variation of edges in the density field and, in particularly, detect the object edges through the final step of hysteresis.

3.3 Second Derivative

Edge detection in images and 3D voxel space can not only be performed based on the first derivative, as it is the case with the

Sobel filter and the extension of the Canny filter. The second derivative provides a basic approach to edge detection based on differences of neighboring values, while edges result from the zero crossings. Since the second derivative is usually sensitive to noises, a previous smoothing of the values is essential.

Laplacian of Gaussian From this point Laplacian of Gaussian filter (Marr and Hildreth, 1980) (LOG), also referred as Marr-Hildreth operator, is suitable. It combines the second derivative with a Gaussian filter in order to smooth the values. For fast implementation the Difference of Gaussians (DoG) can be applied, which approximates the LOG. Similar to the filter of the first derivative, we apply the filter on the voxelized 3D density field and refer it as $\Delta_{\delta, \text{LOG}}^2$ in the following.

3.4 Evaluation

Completeness In general, we report qualitative completeness on the basis of the resulting 3D reconstructions. Furthermore, the completeness is measured quantitatively. The reconstructions from voxelized 3D density field include predicted points inside the object and the reference point cloud contains large gaps. We report the number of points and percentages covered by the NeRF reconstructions within a distance threshold of a maximum distance from reference. A higher score indicates higher object completeness.

Correctness To evaluate the geometric accuracy of the 3D reconstructions quantitative as well as qualitative, Chamfer cloud-to-cloud distance is applied from the DTU dataset evaluation script (Jensen et al., 2014). We report both the distance from data to reference (data-to-reference) and vice versa (reference-to-data). While the reference point cloud has gaps, the data to reference distance as well as the reference to data distance are interpreted as accuracy or correctness.

4. EXPERIMENTS

In this section, we conduct experiments on a challenging benchmark dataset with different types of real objects, which feature different sizes, structures, materials, textures and colors.

4.1 Dataset

For the evaluation of our framework, we use the DTU benchmark dataset (Jensen et al., 2014). The dataset consists of scenes featuring real objects, including images, corresponding camera poses, and reference point clouds obtained from a structured-light scanner (SLS). We specifically focus on six scenes within the dataset, the same as (Wang et al., 2021; Oechsle et al., 2021; Darmon et al., 2022; Li et al., 2023), each containing either 49 or 64 RGB images.

4.2 Implementation

For all investigations, Instant NGP (Müller et al., 2022) was taken into account as NeRF, since it enables real time training and rendering. Regarding the network architecture, the basic NeRF architecture with ReLU activations and hash encoding is selected, while the training incorporates 50 000 training steps on an NVIDIA RTX3090 GPU.

4.3 Experiments

We evaluate our framework with first derivative Sobel filter and Canny filter as well as second derivative Laplacian of Gaussian filter against different global density thresholds. Thereby qualitative as well as quantitative results based on completeness and correctness as described in the evaluation Section 3.4 are considered. The global density thresholds δ_t are set to 25, 50, and 100 (Wang et al., 2021). The Sobel filter is used as described in Section 3.2 and the Canny filter is applied with a standard derivation of 0.1 and relative thresholds of 0.0005 and 4 times 0.0005. For the Laplacian of Gaussian, a filter mask of $7 \times 7 \times 7$ and standard derivation of 7 is utilized.

5. RESULTS

In the following sections, we show qualitative (Section 5.1) and quantitative (Section 5.2) results of the geometric reconstructions on the used benchmark dataset by addressing completeness and correctness.

5.1 Qualitative results

As the following Figures 2 and 4 show, the density gradient-based approach with 3D edge detection filters yields promising results. Thus, the optimal global density threshold varies from scene to scene and requires adaptive adjustment. By addressing the density gradient, consistently accurate and complete results are generated across all scenes.

Completeness The visual comparison of the colored geometric reconstructions in Figure 2 highlights the reconstruction quality and object completeness based on density gradients. The reconstructions exemplified for a global density threshold $\delta_{t=50}$ exhibit different levels of gaps in the point clouds. In almost all scenes, gaps appear in the reconstructions along with areas of extremely high point density. Also the reconstructions resulting from the first derivative, the Sobel filter $\Delta_{\delta, \text{Sobel}}$, performs slightly different depending on the scene. For certain scenes like scan40 and scan55 the detected edges seem to be located too far above the reference surface. For the other scenes, however, substantial gaps exist. The Canny filter $\Delta_{\delta, \text{Canny}}$ provides the strongest visual results. Besides the colorful and smooth objects like scene scan63, also complex collections like in scene scan37 can be reconstructed almost completely. In general, the Canny filter effectively eliminates gaps and delivers a uniform point density. In addition, the subsurface of the scenes containing a colored ground are well captured. The second derivation with the Laplacian of Gaussian $\Delta_{\delta, \text{LOG}}^2$ also reaches a complete reconstruction at first sight. However, especially at scene scan55 and partly scene scan40 the point cloud tends to be rather fuzzy and noisy.

Correctness Besides the visually strong results, the density gradient applications also provide geometrically promising results (Figure 4). Both the global density threshold as well as the gradient filters enable results with accuracies up to 2.5 mm for most parts of the object surfaces. Nevertheless, especially in reconstructions from global density thresholds and Sobel filter $\Delta_{\delta, \text{Sobel}}$, some artifacts up to 10 mm appear. In contrast, the Canny filter $\Delta_{\delta, \text{Canny}}$ provides mainly consistent high accuracies to about 1.5 mm. The geometric accuracy of the Laplacian of Gaussian $\Delta_{\delta, \text{LOG}}^2$ depends highly on the scene and appears quite noisy. Note that edged areas with a large deviation



Figure 2. Qualitative comparison on the real DTU benchmark dataset. Comparison between the reference point clouds and the geometric reconstructions from 3D density field using a global density threshold $\delta_{t=50}$, density gradients from Sobel filter $\Delta_{\delta, \text{Sobel}}$, Canny filter $\Delta_{\delta, \text{Canny}}$ and Laplacian of Gaussian $\Delta_{\delta, \text{LOG}}^2$.

Table 1. **Completeness.** Geometric completeness with the number of points \uparrow in million of the reference with the geometric reconstructions from voxelized 3D density field with global density thresholds δ_t , Sobel filter $\Delta_{\delta, \text{Sobel}}$, Canny filter $\Delta_{\delta, \text{Canny}}$ and Laplacian of Gaussian $\Delta_{\delta, \text{LOG}}^2$ within distance thresholds of a maximum distance of about 0.5 mm, 1.0 mm and 1.5 mm from reference. The percentage \uparrow is shown in brackets. Best results bold in green, second best results bold in blue.

	scan24	scan37	scan40	scan55	scan63	scan114	mean in %
1.5 mm							
$\delta_{t=25}$	3.08 (96.99 %)	2.27 (97.58 %)	2.95 (98.36 %)	2.96 (90.80 %)	1.10 (97.51 %)	3.02 (97.66 %)	96.48
$\delta_{t=50}$	2.98 (93.79 %)	2.10 (90.48 %)	2.86 (95.31 %)	2.35 (72.22 %)	0.87 (77.42 %)	2.79 (90.27 %)	86.58
$\delta_{t=100}$	2.79 (87.90 %)	1.66 (71.54 %)	2.66 (88.51 %)	1.94 (59.53 %)	0.47 (41.71 %)	2.39 (77.17 %)	71.07
$\Delta_{\delta, \text{Sobel}}$	3.03 (95.24 %)	2.03 (87.30 %)	2.88 (96.01 %)	2.09 (63.98 %)	1.02 (90.83 %)	2.40 (77.48 %)	85.14
$\Delta_{\delta, \text{Canny}}$	3.00 (94.43 %)	2.26 (97.28 %)	2.97 (98.93 %)	2.90 (88.91 %)	1.12 (99.49 %)	3.02 (97.54 %)	96.10
$\Delta_{\delta, \text{LOG}}^2$	2.73 (85.76 %)	2.21 (95.08 %)	2.79 (93.11 %)	2.52 (77.15 %)	1.11 (98.30 %)	2.95 (95.33 %)	90.79
1.0 mm							
$\delta_{t=25}$	2.98 (93.60 %)	2.21 (94.89 %)	2.87 (95.80 %)	2.82 (86.43 %)	1.06 (93.80 %)	2.95 (95.55 %)	93.35
$\delta_{t=50}$	2.82 (88.73 %)	1.92 (82.80 %)	2.71 (90.50 %)	2.17 (66.65 %)	0.75 (66.83 %)	2.64 (85.25 %)	80.13
$\delta_{t=100}$	2.52 (79.38 %)	1.41 (60.58 %)	2.43 (80.96 %)	1.86 (57.08 %)	0.36 (32.32 %)	2.11 (68.22 %)	63.09
$\Delta_{\delta, \text{Sobel}}$	2.94 (92.43 %)	1.86 (80.17 %)	2.82 (93.92 %)	2.02 (61.87 %)	0.96 (84.94 %)	2.23 (72.00 %)	80.88
$\Delta_{\delta, \text{Canny}}$	2.46 (77.22 %)	2.08 (89.46 %)	2.73 (91.05 %)	2.27 (69.57 %)	1.10 (98.06 %)	2.87 (92.73 %)	86.35
$\Delta_{\delta, \text{LOG}}^2$	2.13 (66.94 %)	1.93 (83.15 %)	2.17 (72.36 %)	1.98 (60.66 %)	1.03 (91.48 %)	2.57 (83.18 %)	76.30
0.5 mm							
$\delta_{t=25}$	2.63 (82.86 %)	1.81 (77.70 %)	2.28 (75.86 %)	2.20 (67.46 %)	0.92 (81.48 %)	2.73 (88.21 %)	78.93
$\delta_{t=50}$	2.31 (72.66 %)	1.39 (59.63 %)	2.00 (66.74 %)	1.60 (49.03 %)	0.55 (48.97 %)	2.22 (71.66 %)	61.45
$\delta_{t=100}$	1.70 (53.37 %)	0.88 (37.83 %)	1.59 (53.03 %)	1.21 (37.15 %)	0.22 (19.48 %)	1.49 (48.03 %)	41.48
$\Delta_{\delta, \text{Sobel}}$	2.69 (84.67 %)	1.40 (60.12 %)	2.43 (80.86 %)	1.77 (54.22 %)	0.81 (72.39 %)	1.89 (61.00 %)	68.88
$\Delta_{\delta, \text{Canny}}$	1.14 (35.85 %)	1.00 (42.86 %)	1.25 (41.69 %)	0.80 (24.67 %)	0.87 (77.51 %)	1.96 (63.55 %)	47.69
$\Delta_{\delta, \text{LOG}}^2$	1.20 (37.66 %)	1.13 (48.73 %)	0.81 (26.85 %)	1.16 (35.59 %)	0.75 (66.99 %)	1.58 (51.19 %)	44.50

are mainly due to the missing parts of the points in the SLS reference, which are depicted in the images and therefore in the reconstruction from 3D density field.

5.2 Quantitative results

Completeness The reported completeness reached by the different NeRF reconstructions is shown in Table 1 and specified by absolute number of points as well as percentage. Altogether, the completeness values for the distance thresholds up to 1 and 1.5 mm exceed 60 % for all methods. As expected, an increase of the density threshold δ_t causes a decrease of the completeness, due to the fact that a higher number of points are removed. Accordingly, using a density threshold of 25 results in the highest completeness for this dataset, with a mean across scenes of approximately 96 % for points below 1.5 mm and 93 % up to 1 mm accuracy. The results from density gradients through the Canny filter also stands out strongly. On average, 96 % completeness is achieved for 1.5 mm and 86 % for 1 mm. Taking a more detailed look, the methods perform variably for each scene. Canny performs particularly well on complex, specular and smooth objects as in scene scan37, scan63 or scan114. However, at fine detail levels and rough objects like in scene scan24 and scan55, the completeness quickly weakens for highly accurate reconstructions up to 0.5 mm. Nonetheless, the completeness decreases significantly using global density thresholds starting from $\delta_{t=50}$ and can not compete with the Canny filter.

Correctness Since NeRFs estimate values in the entire 3D space and consequently inside the objects, there may be artificial points within the objects, which affect the quantitative accuracy results in terms of correctness. Respectively, the results (Table 2) are mostly in the same, rather coarse, range of accuracies up to 6 mm, from the NeRF reconstructions to the reference (data-to-reference). While using a global threshold performs differently depending on the scene, using density gradi-

ents remains consistently stable across all scenes. Nevertheless, the points within the object undermine the interpretability of the results. To emphasize the accuracy potential of density gradients, considering the reconstruction surface points, Figure 3 shows the surface points below 0.5, 1.0 and 1.5 mm for a result based on the Canny filter. It illustrates that the Canny filter approach generates a densely sampled scene whose surface points exhibit high geometric accuracies. When viewing the accuracy from the reference to the 3D reconstructions (reference-to-data), the density gradients stand out positively with an achieved correctness compared to the global density thresholds as well.

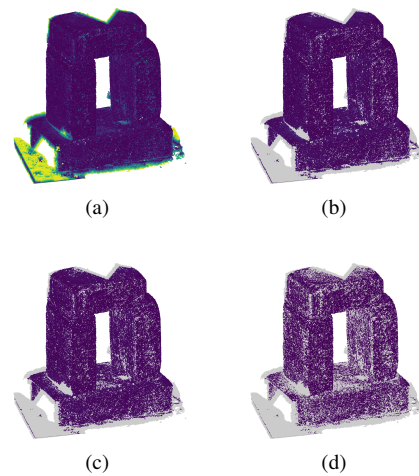


Figure 3. Extraction of surface points (colored) of a reconstruction using Canny filter below a accuracy of (a) 10.0 mm, (b) 1.5 mm, (c) 1.0 mm, and (d) 0.5 mm. Points beyond are grey. The surface points show a high spatial density combined with a high geometric accuracy.

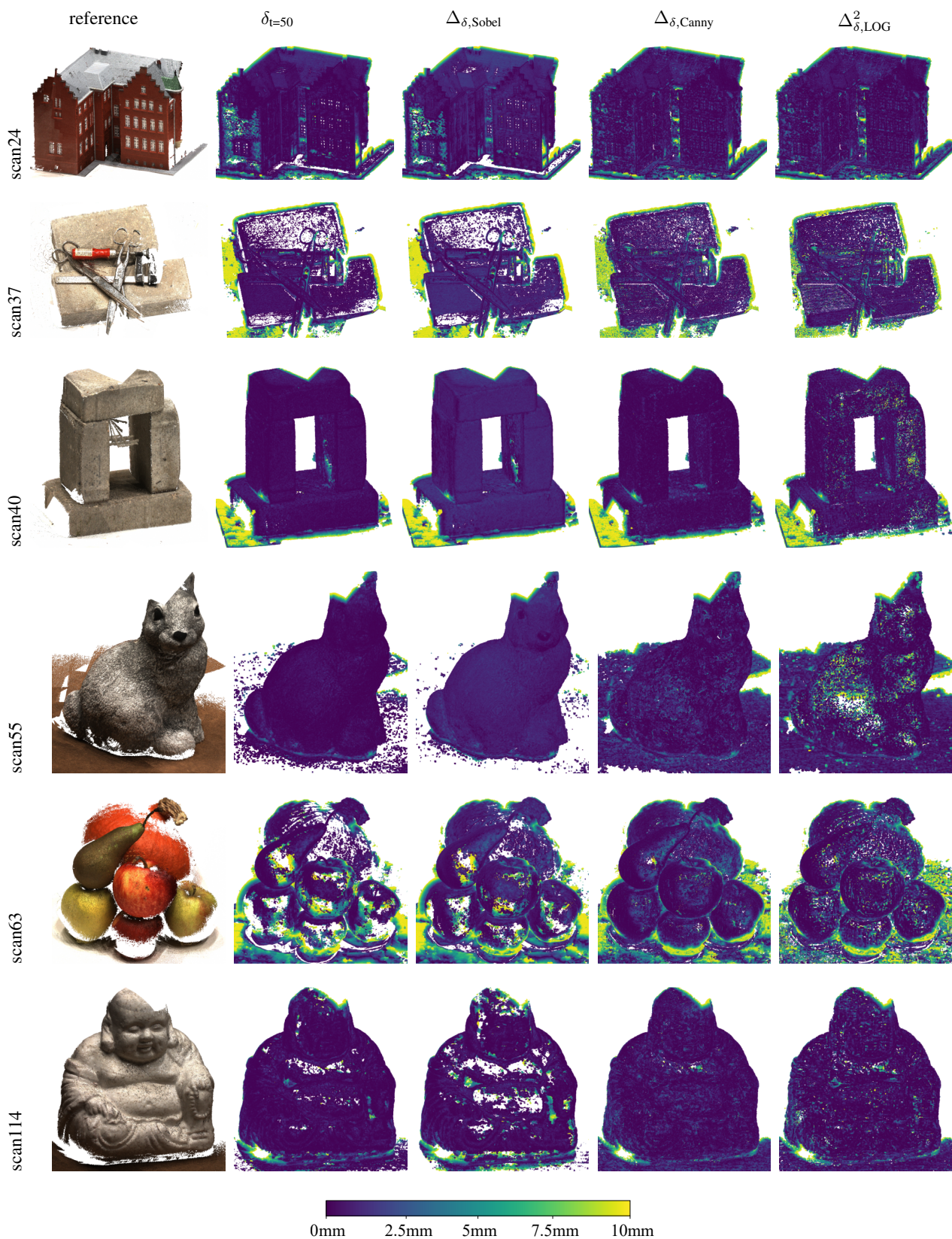


Figure 4. Qualitative comparison on the real DTU benchmark dataset with Chamfer cloud-to-cloud distances. Comparison between the reference point clouds and the geometric reconstructions from 3D density field using a global density threshold $\delta_{t=50}$, density gradients from Sobel filter $\Delta_{\delta, \text{Sobel}}$, Canny filter $\Delta_{\delta, \text{Canny}}$ and Laplacian of Gaussian $\Delta_{\delta, \text{LOG}}^2$.

Table 2. **Correctness.** Geometric accuracy with Chamfer cloud-to-cloud distance \downarrow in mm of the geometric reconstructions from voxelized 3D density field with global density thresholds δ_t , Sobel filter $\Delta_{\delta, \text{Sobel}}$, Canny filter $\Delta_{\delta, \text{Canny}}$ and Laplacian of Gaussian $\Delta_{\delta, \text{LOG}}^2$. From data-to-reference as well as reference-to-data. For comparable results, we use the same random permuted 2 500 000 points, since the resulting reconstructions include different numbers of points and consequently spatial point density. Best results bold in green, second best results bold in blue.

	scan24	scan37	scan40	scan55	scan63	scan114	mean
data-to-reference (mm)							
$\delta_{t=25}$	3.26	5.31	3.53	3.02	5.93	3.21	4.04
$\delta_{t=50}$	2.86	5.63	3.44	3.34	6.08	2.84	4.03
$\delta_{t=100}$	3.08	6.05	3.35	3.48	6.25	3.28	4.25
$\Delta_{\delta, \text{Sobel}}$	2.79	5.65	3.31	3.12	6.20	2.72	3.97
$\Delta_{\delta, \text{Canny}}$	3.03	5.26	3.62	2.76	5.87	2.85	3.89
$\Delta_{\delta, \text{LOG}}^2$	3.40	3.98	3.44	2.06	5.65	2.57	3.52
reference-to-data (mm)							
$\delta_{t=25}$	0.82	0.64	0.76	0.64	0.82	1.95	0.94
$\delta_{t=50}$	0.79	0.82	0.81	0.60	1.50	0.63	0.86
$\delta_{t=100}$	1.05	1.38	0.99	0.63	3.97	2.43	1.74
$\Delta_{\delta, \text{Sobel}}$	0.76	0.96	0.77	0.57	1.02	0.77	0.81
$\Delta_{\delta, \text{Canny}}$	0.91	0.67	0.79	1.02	0.70	0.70	0.80
$\Delta_{\delta, \text{LOG}}^2$	1.09	0.68	0.95	1.27	0.74	0.88	0.93

6. DISCUSSION

In this paper, we investigate the density gradients for achieving high geometric completeness and correctness in 3D reconstructions based on density gradients from NeRFs density output. The application of gradient filters on the density field for 3D edge detection shows remarkable results, compared to the usage of global density thresholds. The latter often leads to gaps or artifacts in the reconstructions, depending on the chosen threshold. However, by extracting surfaces based on density gradients, we can overcome this issue.

The qualitative results of the density gradients, especially by the Canny filter, consistently stand out as positive over all scenes in terms of completeness, this aligns with both quantitative and qualitative results. While global density thresholds yield good results, scene-dependent accuracy variations exist. For some scenes the Sobel filter as well as Laplacian of Gaussian also serve as suitable results and are alternatives to global density thresholds. Nevertheless, the improvements with the Canny filter for object edge detection outperform the other techniques, ensuring nearly gapless reconstructions for objects and subsurface in all scenes. The trade-off between correctness and completeness with global density thresholds is evident: Lower density thresholds lead to higher completeness but not necessarily superior correctness. The density gradients, especially based on the Canny filter, strike a favorable balance between correctness and completeness across the scenes.

Although our framework achieves high accuracy on the object surfaces, it should be noted that points exist within the objects due to the addressing of the whole voxelized density field. These artifactual points distort the quantitative correctness and do not contribute to the visual appearance and surface accuracy. Limitations are given by processing within the entire density grid thus causing artifacts within the object. This issue may be addressed by extracting only the surface, e.g., using convex hull algorithms. In addition, we aim to apply neural methods for 3D edge detection.

The range and values of the density among different NeRFs, hyperparameters, network configurations, and scenes is variable. Dealing with absolute density values presents a challenge. The density gradients are almost independent of absolute density magnitudes and relying on relative neighboring values in

all directions by applying 3D edge detection filter. A notable advantage of our approach is its applicability to different applications. Density gradients allow us to extract surfaces along lower density values using 3D edge detection filters such as Sobel, Canny and Laplacian of Gaussian.

7. CONCLUSION

In summary, we have demonstrated that density gradients based geometric reconstructions lead to high completeness and adequate accuracy. In considering specific relative density variations or gradients based on first and second derivatives, our approach shows potential for application to various NeRFs, that allow the extraction of a regular voxelized density field. This makes our approach rather independent from absolute NeRFs density output. Furthermore, by filtering with global density thresholds, the points are emphasized individually and independently. In contrast, the utilization of 3D gradient filters leverages the inclusion of gradient-based neighborhood information in an anisotropic manner. Therefore, our approach provides a promising anisotropic solution for complete 3D reconstruction from NeRF with high geometric accuracy. Consequently, our method introduces a promising, from absolute density magnitude independent solution, which opens new possibilities of reconstructions using NeRFs.

References

- Canny, J., 1986. A computational approach to edge detection. *IEEE Transactions on pattern analysis and machine intelligence*, 679–698.
- Chng, S.-F., Ramasinghe, S., Sherrah, J., Lucey, S., 2022. Gaussian activated neural radiance fields for high fidelity reconstruction and pose estimation. *European Conference on Computer Vision (ECCV)*, 264–280.
- Darmon, F., Basclé, B., Devaux, J.-C., Monasse, P., Aubry, M., 2022. Improving neural implicit surfaces geometry with patch warping. *Proceedings of the IEEE/CVF Conference on Computer Vision and Pattern Recognition*, 6260–6269.

- Fridovich-Keil, S., Yu, A., Tancik, M., Chen, Q., Recht, B., Kanazawa, A., 2022. Plenoxels: Radiance fields without neural networks. *Proceedings of the IEEE/CVF Conference on Computer Vision and Pattern Recognition*, 5501–5510.
- Gao, C., Saraf, A., Kopf, J., Huang, J.-B., 2021. Dynamic view synthesis from dynamic monocular video. *Proceedings of the IEEE/CVF International Conference on Computer Vision*, 5712–5721.
- Garbin, S. J., Kowalski, M., Johnson, M., Shotton, J., Valentin, J., 2021. Fastnerf: High-fidelity neural rendering at 200fps. *Proceedings of the IEEE/CVF International Conference on Computer Vision*, 14346–14355.
- Jäger, M., Hübner, P., Haitz, D., Jutzi, B., 2023. A comparative Neural Radiance Field (NeRF) 3D analysis of camera poses from HoloLens trajectories and Structure from Motion. *International Archives of the Photogrammetry, Remote Sensing & Spatial Information Sciences*, 48.
- Jensen, R., Dahl, A., Vogiatzis, G., Tola, E., Aanæs, H., 2014. Large scale multi-view stereopsis evaluation. *2014 IEEE Conference on Computer Vision and Pattern Recognition*, IEEE, 406–413.
- Kurz, A., Neff, T., Lv, Z., Zollhöfer, M., Steinberger, M., 2022. Adanerf: Adaptive sampling for real-time rendering of neural radiance fields. *European Conference on Computer Vision (ECCV)*, 254–270.
- Li, Z., Müller, T., Evans, A., Taylor, R. H., Unberath, M., Liu, M.-Y., Lin, C.-H., 2023. Neuralangelo: High-fidelity neural surface reconstruction. *IEEE Conference on Computer Vision and Pattern Recognition (CVPR)*.
- Lin, C.-H., Ma, W.-C., Torralba, A., Lucey, S., 2021. Barf: Bundle-adjusting neural radiance fields. *Proceedings of the IEEE/CVF International Conference on Computer Vision*, 5741–5751.
- Marr, D., Hildreth, E., 1980. Theory of edge detection. *Proceedings of the Royal Society of London. Series B. Biological Sciences*, 207(1167), 187–217.
- Mildenhall, B., Srinivasan, P. P., Tancik, M., Barron, J. T., Ramamoorthi, R., Ng, R., 2020. NeRF: Representing Scenes as Neural Radiance Fields for View Synthesis. *European Conference on Computer Vision (ECCV)*, 405–421.
- Müller, T., Evans, A., Schied, C., Keller, A., 2022. Instant Neural Graphics Primitives with a Multiresolution Hash Encoding. *ACM Transactions on Graphics*, 41(4), 102:1-15.
- Oechsle, M., Peng, S., Geiger, A., 2021. Unisurf: Unifying neural implicit surfaces and radiance fields for multi-view reconstruction. *Proceedings of the IEEE/CVF International Conference on Computer Vision*, 5589–5599.
- Park, J. J., Florence, P., Straub, J., Newcombe, R., Lovegrove, S., 2019. DeepSDF: Learning continuous signed distance functions for shape representation. *Proceedings of the IEEE/CVF conference on computer vision and pattern recognition*, 165–174.
- Pumarola, A., Corona, E., Pons-Moll, G., Moreno-Noguer, F., 2021. D-nerf: Neural radiance fields for dynamic scenes. *Proceedings of the IEEE/CVF Conference on Computer Vision and Pattern Recognition*, 10318–10327.
- Sitzmann, V., Zollhöfer, M., Wetzstein, G., 2019. Scene representation networks: Continuous 3d-structure-aware neural scene representations. *Advances in Neural Information Processing Systems*, 32.
- Sobel, I., Feldman, G., 1973. A 3×3 isotropic gradient operator for image processing. *Pattern Classification and Scene Analysis*, 271-272.
- Tancik, M., Casser, V., Yan, X., Pradhan, S., Mildenhall, B., Srinivasan, P. P., Barron, J. T., Kretzschmar, H., 2022. Blocknerf: Scalable large scene neural view synthesis. *Proceedings of the IEEE/CVF Conference on Computer Vision and Pattern Recognition*, 8248–8258.
- Turki, H., Ramanan, D., Satyanarayanan, M., 2022. Mega-nerf: Scalable construction of large-scale nerfs for virtual fly-throughs. *Proceedings of the IEEE/CVF Conference on Computer Vision and Pattern Recognition*, 12922–12931.
- Wang, P., Liu, L., Liu, Y., Theobalt, C., Komura, T., Wang, W., 2021. Neus: Learning neural implicit surfaces by volume rendering for multi-view reconstruction. *Advances in Neural Information Processing Systems*, 34, 27171–27183.
- Yariv, L., Gu, J., Kasten, Y., Lipman, Y., 2021. Volume rendering of neural implicit surfaces. *Advances in Neural Information Processing Systems*, 34, 4805–4815.